Extreme Mechanics Letters 21 (2018) 65–75

Contents lists available at ScienceDirect

Extreme Mechanics Letters

journal homepage: www.elsevier.com/locate/eml

The mechanical and electrical properties of direct-spun carbon nanotube mats

J.C. Stallard [a,*], W. Tan [a], F.R. Smail [a], T.S. Gspann [b], A.M. Boies [a], N.A. Fleck [a]

[a] Department of Engineering, University of Cambridge, Trumpington Street, Cambridge, CB2 1PZ, UK
[b] Department of Materials Science & Metallurgy, University of Cambridge, 27 Charles Babbage Road, Cambridge, CB3 0FS, UK

ARTICLE INFO

Article history:
Received 29 January 2018
Received in revised form 21 March 2018
Accepted 22 March 2018
Available online 27 March 2018

Keywords:
Carbon nanotube mat
Mechanical properties
In-situ testing
Nanotube bundles

ABSTRACT

The mechanical and electrical properties of a direct-spun carbon nanotube mat are measured. The mat comprises an interlinked random network of nanotube bundles, with approximately 40 nanotubes in a bundle. A small degree of in-plane anisotropy is observed. The bundles occasionally branch, and the mesh topology resembles a 2D lattice of nodal connectivity slightly below 4. The macroscopic in-plane tensile response is elasto-plastic in nature, with significant orientation hardening. In-situ microscopy reveals that the nanotube bundles do not slide past each other at their junctions under macroscopic strain. A micromechanical model is developed to relate the macroscopic modulus and flow strength to the longitudinal shear response of the nanotube bundles. The mechanical and electrical properties of the mat are compared with those of other nanotube arrangements over a wide range of density.

© 2018 The Authors. Published by Elsevier Ltd. This is an open access article under the CC BY license (http://creativecommons.org/licenses/by/4.0/).

1. Introduction

Individual carbon nanotubes (CNTs) possess exceptional mechanical and electrical properties [1]. The walls of CNTs have a Young's modulus of 1 TPa and a tensile strength of approximately 100 GPa [2], whilst isolated CNTs possess electrical conductivities of 2×10^7 s/m [3], ampacity of 10^{13} A/m^2 [4], and thermal conductivity of 3500 W/mK [5]. These properties are sufficiently impressive that significant research and industrial interest has arisen in the development of materials with CNTs as their primary constituents, and suitable for manufacture in industrial quantities. The *'Windle Process'* involves spinning a CNT aerogel from a gas phase, and has received much attention since the method was introduced by Li et al. [6] in 2004.

Methods for producing CNT materials may be divided into three families, together resulting in eight different types of CNT material. Fig. 1 illustrates the three families, the methods which comprise them, and their morphologies. The first family involves processing vertically aligned CNTs grown from substrates by chemical vapour deposition; these CNT 'forests' may be (i) densified into pillars, (ii) spun into 1-dimensional fibres, or (iii) drawn into aligned 2-dimensional mats. The second family utilises liquids to create suspensions or solutions of short, mass-produced CNTs. CNT-solvent solutions can be filtered to create (iv) random planar 'buckypaper' mats, or spun into coagulating fluids to produce (v) single fibres. Porous CNT foams (vi) are often produced from aqueous gel precursors by critical point drying, or freeze drying. The final family uses direct-spun carbon nanotube aerogels, produced via the 'Windle process'. Direct-spun fibres (vii) are produced by on-line solvent-condensation of the aerogels; alternatively, the spinning of aerogel layers onto a rotating mandrel, with or without solvent condensation, produces direct-spun mats, labelled (viii).

Charts that summarise the elastic moduli, strength, and electrical and thermal conductivity as a function of density for these CNT-based materials are presented in Fig. 2. Note that the bulk density of CNT materials ranges from a few kg/m^3 for CNT foams to over 1000 kg/m^3 for CNT fibres, whilst their moduli range from tens of kPa to hundreds of GPa. Large differences in strength and conductivity are also observed. Wide property variations occur between classes and also within individual material classes. For example, direct-spun materials exhibit a large variation in mechanical properties due to their range of material alignment and density [7].

The macroscopic modulus of CNT materials is much below the Voigt upper bound, based on the in-plane modulus of a CNT wall (i.e. graphene). A similar observation can be made for strength as follows. If the ultimate tensile strength of CNT walls is assumed to be 100 GPa, all CNT morphologies lie more than an order of magnitude below the Voigt bound for ultimate tensile strength, as illustrated in Fig. 2(b). In broad terms, the moduli and compressive yield strength of CNT foams and CNT forest based materials appear to scale with density ρ according to $E \sim \rho^3$ and $\sigma \sim \rho^2$ respectively. This scaling law is representative of cellular solids of low nodal connectivity [8].

* Corresponding author.
E-mail address: jcs202@cam.ac.uk (J.C. Stallard).

https://doi.org/10.1016/j.eml.2018.03.003
2352-4316/© 2018 The Authors. Published by Elsevier Ltd. This is an open access article under the CC BY license (http://creativecommons.org/licenses/by/4.0/).

The modulus and ultimate tensile strength of aligned CNT materials, such as fibres spun from solution and mats drawn from CNT arrays, vary by up to two orders of magnitude for a given density. Electrical conductivity also exhibits considerable variation between categories and also within individual categories. In the case of fibres spun from solution, a high electrical conductivity close to the Voigt bound is possible due to doping by acids, or by treatment with iodine [9]. The specific electrical conductivities of these materials are close to those of metallic alloys.

Now consider the chart of thermal conductivity versus density, see Fig. 2(d). Aside from CNT foams, all categories of CNT materials have exceptionally high thermal conductivity compared to most other engineering solids. A line of specific thermal conductivity $\kappa/\rho = 0.0449\,\mathrm{m}^4/\mathrm{Ks}^3$, equal to that of pure copper, has been added to Fig. 2(d). This line lies well below that of many CNT materials.

Fig. 3 presents a schematic of the continuous manufacturing method for direct-spun CNT materials as used in the present study, and the typical microstructure of CNT mat. A carbon source, often methane, is mixed with iron and sulphur catalysts and a carrier gas, typically hydrogen, in a furnace at 1570 K [10]. The catalysts initially vaporise but later, as the mixture cools, iron nanoparticles recondense out of the gas phase. The iron particles grow, and develop a sulphur coating [11]. Fullerene caps form on the surface of the nanoparticles, and the fullerene caps then evolve into individual CNTs [12], and these in turn bind together into a network of CNT bundles by van-der-Waals attraction [11]. This network forms a cylindrical aerogel 'sock', and the sock is drawn from the reactor by winding it onto a mandrel. The degree of anisotropy in direct-spun CNT materials is sensitive to the ratio of draw speed to velocity of gas flow [7]. Many layers of drawn CNT aerogel stack to form a carbon nanotube mat. Immersion in a solvent, typically acetone, followed by evaporation, results in capillary condensation and a thinner, denser sheet [13].

Direct-spun mats exhibit three distinct hierarchies of microstructure, as illustrated in Fig. 4: the carbon nanotube, nanotube bundle, and the interlinked bundle network [14]. Although CNT bundles possess high tensile strength and stiffness in the axial direction [15], the weak van-der-Waals bonds between adjacent CNTs endow the bundles with a low longitudinal shear modulus and strength [16–18]. The interfacial shear strength between neighbouring CNTs within a bundle varies from 0.04 MPa to 70 MPa as a result of defects within the walls [19,20], and the additional presence of a polymer coating inherent to the chemical vapour deposition process can raise the inter-bundle shear-strength to 400 MPa [21,22].

While microscopy studies of CNT mats during interrupted tensile tests [22–25] have shed light on microstructural changes in CNT mats due to strain, they do not inform us about the deformation mechanisms. To do so, in-situ observation is needed of microstructure evolution during tensile testing. In this study, we measure the nonlinear stress–strain response, piezoresistive behaviour [26] and electrical, physical and chemical properties of a commercially available direct-spun CNT mat. In-situ tensile tests reveal that the bundles undergo bending (and longitudinal shear) without slippage at junctions. A micromechanical model is then developed to relate the mechanical properties of the bundle network to those of individual bundles.

2. Materials and methods

Direct-spun CNT mat was provided by Tortech Nano Fibers Ltd.[1] Before characterisation, the mat was immersed in acetone for 5 min, dried in air for 20 min, and heated at 70 °C for 1 h, to ensure that it was in the fully condensed state. The mat has a nominal thickness of 60 μm, as confirmed by optical interferometry and micrometre measurements. The areal mat density is $0.0234\,\mathrm{kg/m}^2$, and the volumetric mat density is $\rho_{Mat} = 390\,\mathrm{kg/m}^3$. The chemical composition of the direct-spun mat was determined by thermogravimetric and Raman analysis, as described in Appendix A; the results revealed an Fe content of 6 wt.%, remainder CNT. A bundle density of $\rho_B = 1560\,\mathrm{kg/m}^3$ was determined by helium pycnometry; It follows immediately that the relative density of the mat is $\overline{\rho} = \rho_{Mat}/\rho_B = 0.25$. Additional details of helium pycnometry are given in Appendix A.

Uniaxial tensile tests were performed using a screw-driven test machine, with the loading direction inclined at 0°, 45° and 90° to the draw direction of the CNT mat onto the mandrel. The test set-up is shown in Fig. 5(a). The in-plane strain state was measured in the central portion of the sample by tracking the movement of dots of white paint applied prior to testing, using a digital camera and image processing software. Roller-grips enabled high tensile strains to be reached, with failure occurring at a strain level of 20% to 30%. In-situ tensile tests were conducted with a micro-test stage equipped with a 2N load cell, inside a scanning electron microscope (SEM).

The in-plane toughness G_c was measured by a trouser-tear test [27], illustrated in Fig. 5(b). This toughness is determined from the steady state load for tearing, P_t, and the sample thickness, t_s, according to $G_c = 2P_t/t_s$ [28]. Trouser-tear tests were attempted in two directions, with the tear direction aligned with the draw direction, and in the transverse in-plane direction. Additionally, the out-of-plane delamination toughness, G_d, was quantified by a peel test [29], as illustrated in Fig. 5(c). The toughness G_d is related to the peel force P_d and the sample width w_s according to $G_d = 2P_d/w_s$.

Now consider the measurement of electrical properties. The in-plane and through-thickness electrical conductivity were measured using a 4-point probe method, as illustrated in Fig. 6. A 4-point probe was also used to measure the in-plane electrical resistance during tensile testing, at a strain rate of $\dot{\epsilon} = 10^{-4}\,\mathrm{s}^{-1}$. The tensile strain and in-plane resistance were measured with full, partial and cyclic unloading of stress, and a limited number of creep tests at constant stress were also performed.

3. Results

3.1. Uniaxial tensile response

The nominal stress–strain response, as illustrated in Fig. 7(a), exhibited an initial linear behaviour, followed by a strain-hardening plastic response at approximately 4% strain. Above 15% strain, the hardening rate increases. The response has a moderate degree of anisotropy. The in-plane transverse strain is plotted as a function of tensile strain in Fig. 7(b). The apparent Poisson's ratio, ν_{12}, initially equals 0.6, but increases to between 2.7 and 3.5 at higher strains. An explanation for these high values of ν_{12} is evident from images taken during in-situ tensile testing, see Fig. 7(c), which illustrate the appearance of out-of-plane wrinkles at the micron level. This wrinkling appears to contribute to the compressive transverse strain. No noticeable rate dependency was observed for strain rates between $10^{-4}\,\mathrm{s}^{-1}$ and $10^{-2}\,\mathrm{s}^{-1}$, as illustrated in Fig. 7(d) for samples aligned with the draw direction.

3.2. Toughness

Trouser-tear tests along the draw direction were performed from starter cracks cut parallel to the draw direction. The average

[1] Tortech Nano Fibers Ltd, Hanassi Herzog St., Koren Industrial park, Ma'alot Tarshiha, 24952 Israel.

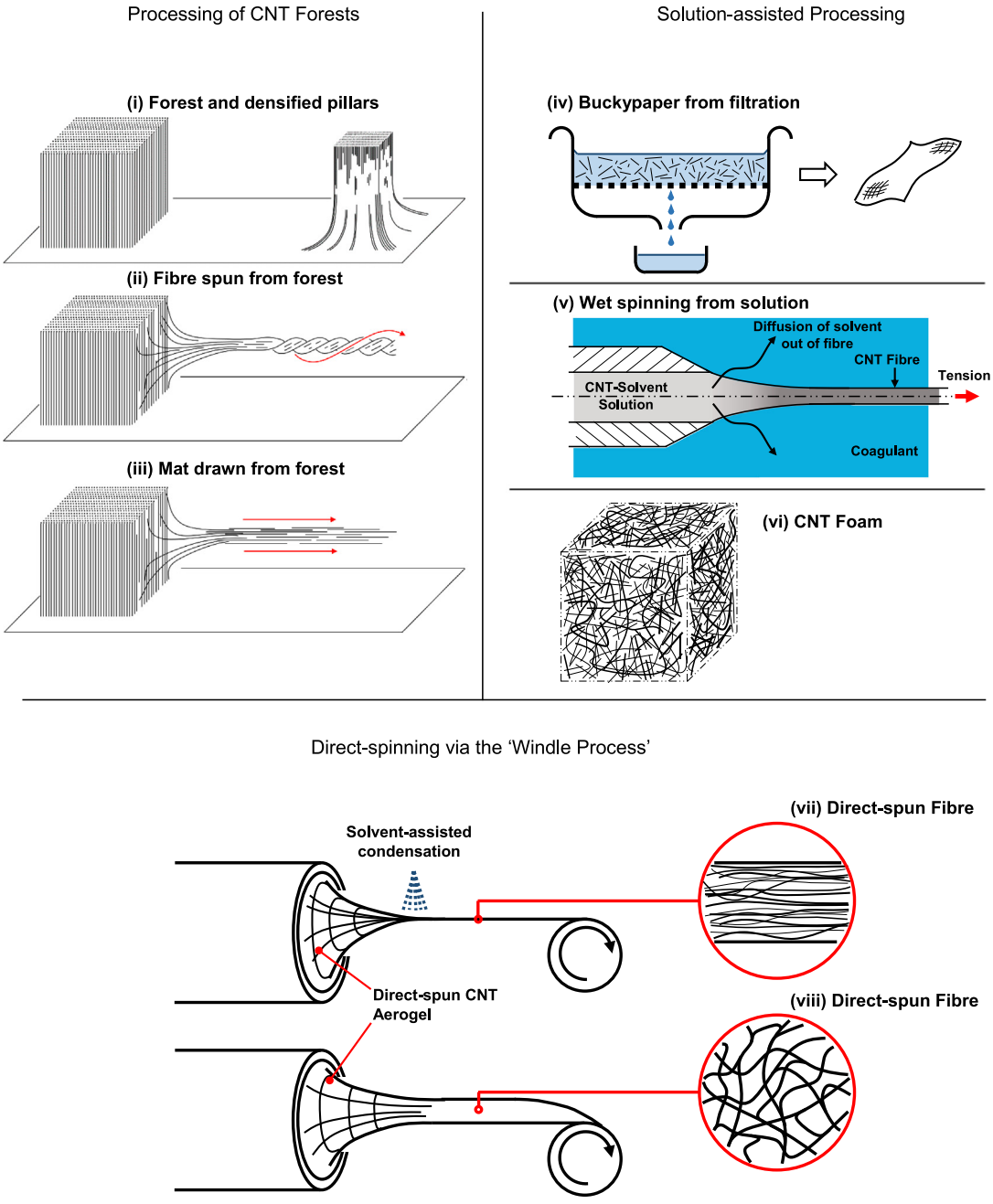

Fig. 1. Classes of bulk CNT materials and production methods.

value of tear energy from these trouser tests was $G_c = 22$ kJ/m^2. Trouser-tests were unable to grow cracks transverse to the draw direction; instead, kinking of the starter crack occurred and no useful data were obtained. The delamination toughness from a peel test was found to be $G_d = 5.4$ J/m^2. This is about four orders of magnitude below the in-plane toughness.

3.3. Electrical properties

The in-plane conductivity exhibited a small degree of anisotropy, with values of 404 S/cm parallel to the manufacturing draw direction, 358 S/cm at 45°, and 325 S/cm at 90°. In the through-thickness direction, electrical conductivity was about 6 orders of magnitude lower, at 6.39×10^{-4} S/cm.

3.4. Unloading response and creep tests

A 4-point probe, as illustrated in Fig. 8(a), was used to measure the in-plane electrical resistance during tensile testing, at a strain rate of $\dot{\epsilon} = 10^{-4}$ s^{-1}. The tensile strain and in-plane resistance were measured with full, partial and cyclic unloading of stress, and also at constant stress. Typical responses are presented, with sample resistance normalised by the initial resistance R_0.

The stress–strain and resistance-strain response with periodic partial unloading of samples at 0°, 45° and 90° to the draw direction are illustrated in Fig. 8(b). Despite the presence of structural anisotropy, the piezoresistive response, R/R_0 versus ϵ_{11}, is qualitatively similar for all directions. Little mechanical or electrical hysteresis is present upon partial unloading. We define the unloading stiffness E_U during the unloading cycle as $E_U = \Delta\sigma_{11}/\Delta\varepsilon_{11}$, where $\Delta\sigma_{11}$ is the change in nominal stress during unloading and $\Delta\varepsilon_{11}$

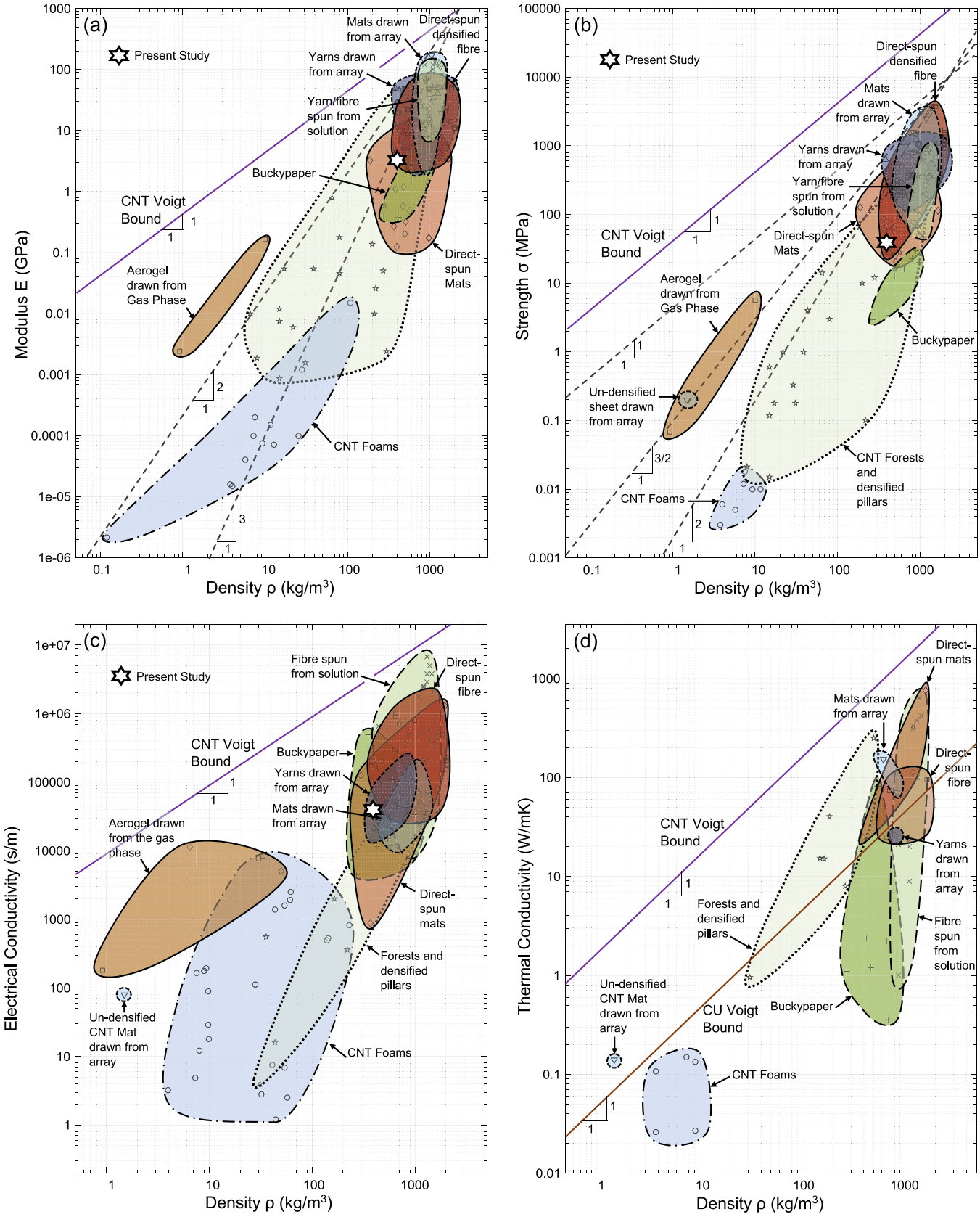

Fig. 2. Property charts of CNT materials: (a) modulus vs density, (b) strength vs density, (c) electrical conductivity vs density, (d) thermal conductivity vs density. References for the experimental data used in these property charts are given in the supplementary material.

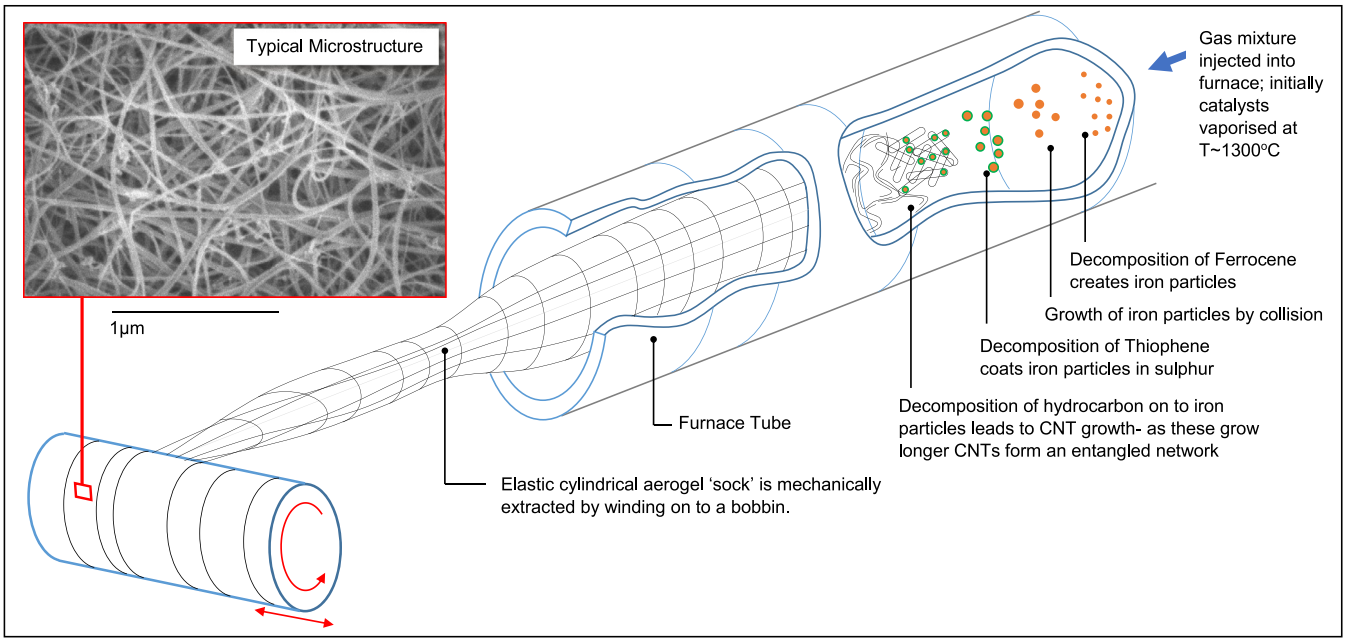

Fig. 3. The 'Windle Process' for producing direct-spun CNT mat, and typical microstructure [6,7,10,11].

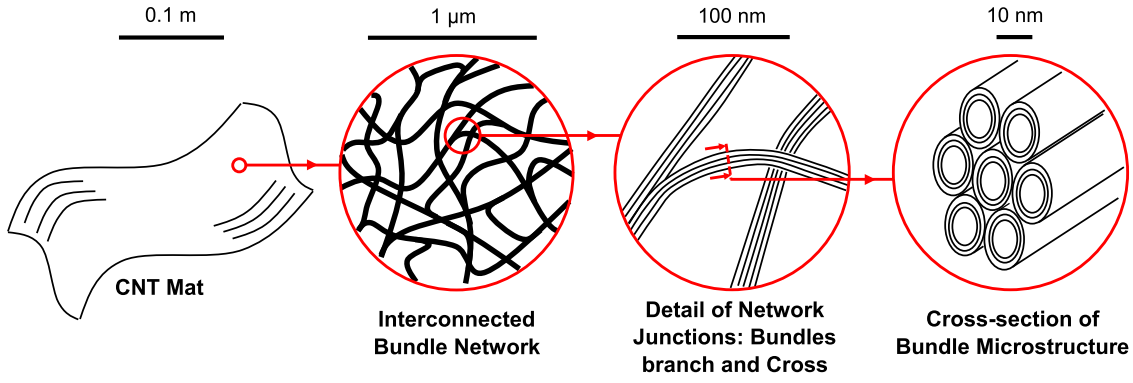

Fig. 4. The hierarchical microstructure of direct-spun CNT mat.

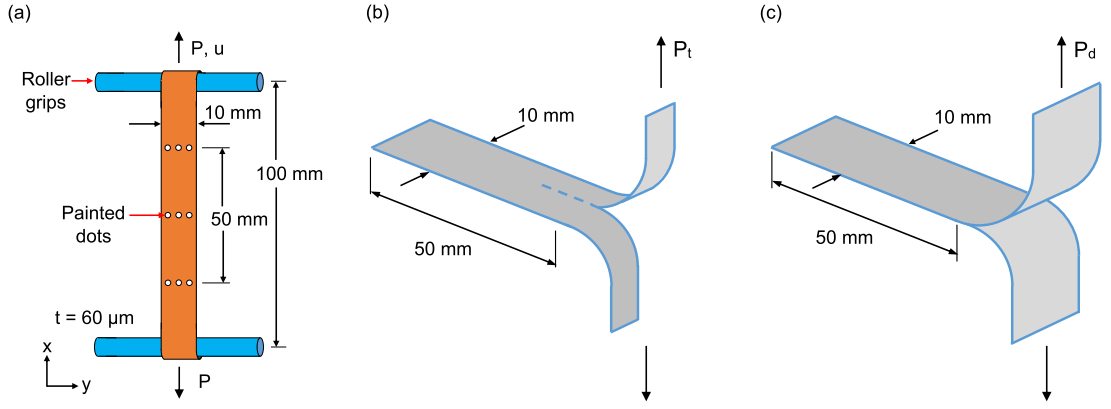

Fig. 5. Mechanical testing techniques: (a) schematic of tensile test setup with sample dimensions and strain measurement techniques. (b) In-plane fracture 'trouser tear' test, (c) delamination peel test.

is the corresponding change in true strain. The gauge factor, GF, is defined as $GF = \Delta (R/R_0) / \Delta \varepsilon_{11}$, where $\Delta(R/R_0)$ is the change in normalised sample resistance during the unloading cycle. The unloading stiffness and gauge factor are plotted against nominal

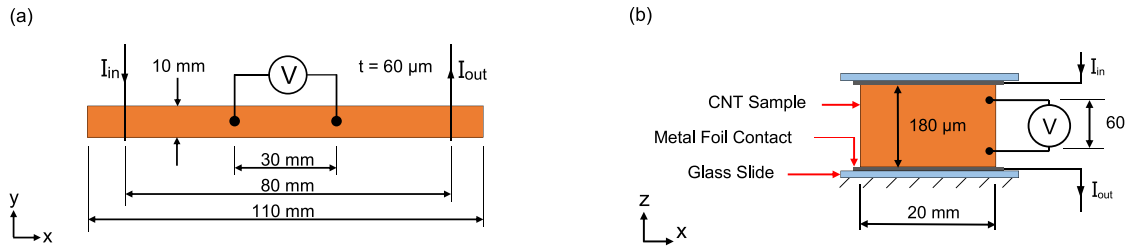

Fig. 6. Four point probe measurement for (a) in-plane and (b) out of plane electrical conductivity.

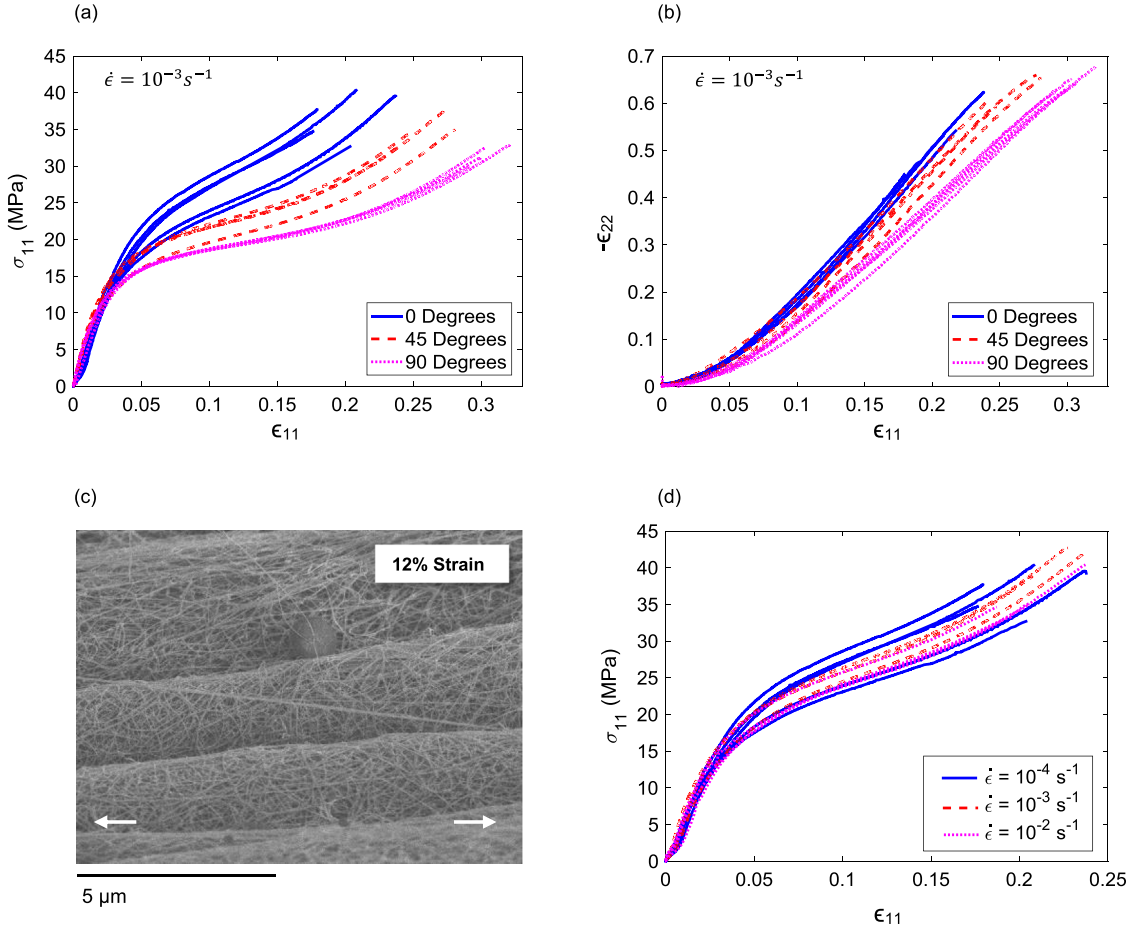

Fig. 7. Uniaxial tensile response: (a) in-plane stress–strain response for different material orientations, (b) relationship between tensile and transverse strains. (c) illustrates the appearance of transverse wrinkles during in-situ tensile testing; the arrows indicate the direction of tensile straining. (d) records the effect of strain rate on the uniaxial tensile response for samples aligned with the draw-direction.

strain in Fig. 8(c). E_U increases with strain for all sample orientations, with the initial rate of increase highest for the 0° samples. The gauge factor during unloading also increases with strain.

Fig. 8(d) illustrates the effect of full unloading for a sample oriented at 0° to the draw direction. Both the resistance-strain and stress–strain responses exhibit hysteresis, and both a permanent strain and permanent change in sample resistance are evident upon unloading.

A stable response to cyclic stress is of importance in many sensing and structural applications. An initial exploration into the response under cyclic uniaxial loading was conducted by applying four loading packets of ten unloading cycles, with results as illustrated in Fig. 8(e). The loading packets labelled 1, 2, and 3 all resulted in permanent drift in the piezoresistive and stress–strain responses. The last set of loading cycles involved cyclic excursions well below the current yield strength, as denoted by the symbol $\Delta\sigma$ in Fig. 8(e). This loading packet gave rise to an elastic response.

The creep behaviour of the CNT mat was investigated by holding a sample at a constant tensile stress of 8.3 MPa, 17 MPa, and then at 25 MPa, each time for 1500 s, before unloading the sample to 17 MPa for a further 1500 s. The strain, ϵ_{11}, recorded at each of these constant stresses is plotted against time in Fig. 8(f). No noticeable creep was observed in the final phase of holding at 17 MPa. Also, no noticeable change in electrical resistance occurred whilst the sample was held at constant stress.

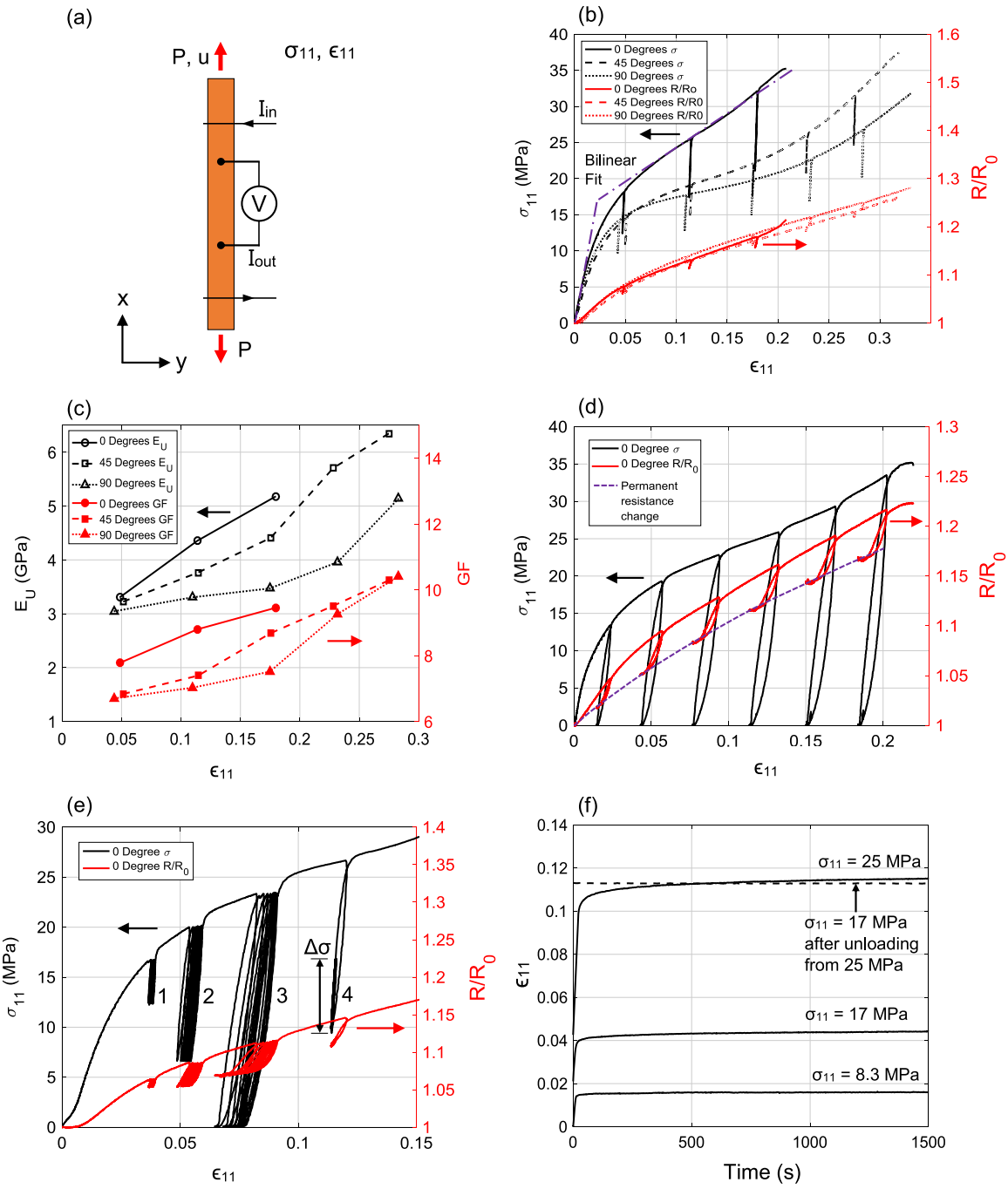

Fig. 8. Nonlinear and piezoresistive behaviour of carbon nanotube mat: (a) schematic of tensile test setup with four point probe, (b) anisotropic response with partial unloading, (c) unload modulus and gauge factor as a function of applied strain for different sample orientations to the draw-direction, (d) full unloading cycles revealing permanent strains and resistance change, (e) drift and hysteresis under cyclic loading, and (f) creep curves showing the effects of constant stress on the tensile strain. Unless otherwise stated, stresses and strains are nominal, as calculated from initial sample dimensions.

3.5. In-situ observations of deformation mechanisms

An understanding of the origin of mechanical properties in direct-spun mats is aided by observation of the deformation mechanisms at the microstructural scale. Unlike other in-situ studies of CNT mats that have been reported in the literature [24,25], in the present study the same microstructural area is observed before and after deformation. This enables us to identify the main mechanisms of deformation. For example, images of microstructure are presented in Fig. 9(a) and (b), for strains of $\epsilon = 0\%$, and 10% respectively, with specific bundles and locations of interest annotated. The bundles labelled 1 and 2 straighten and orient along the loading direction, whereas the transverse bundle labelled 3 undergoes buckling.

4. A model for in-plane mechanical properties

There is a major deficit in stiffness and strength when one compares individual CNTs with bulk CNT materials. In the case of direct-spun mats, why does a random, interconnected network of CNT bundles possess inferior tensile properties to those of individual CNTs? This question is addressed via the model below.

At the microstructural level, the junctions between CNT bundles are of low nodal connectivity, of between 3 and 4. Consequently,

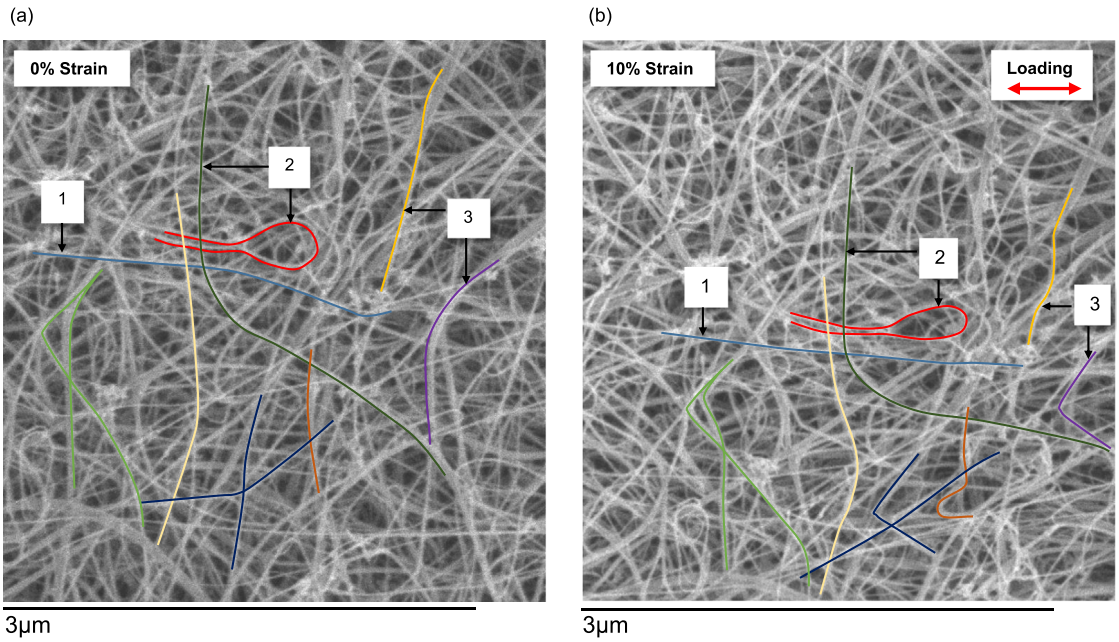

Fig. 9. Microstructural changes during yield: (a) shows a piece of CNT mat microstructure prior to loading, and (b) at 10% macroscopic strain, with bundles and areas of interest highlighted for discussion.

the mechanical properties are governed by the bending and shear response of CNT bundles, rather than by axial stretch [30]. For an approximate prediction of stiffness and strength, this justifies the use of a periodic 2D honeycomb unit cell, as illustrated in Fig. 10(a), with struts of thickness t and length l that deform by bending and shearing [8,30]. CNT bundles form the struts of this unit cell, and are connected to one another at nodes by the exchange of nanotubes from one bundle to the next. We write the relative density of the network $\overline{\rho} = \rho_{Mat}/\rho_B$ as [8]:

$$\overline{\rho} = \frac{3}{2\cos\omega(1+\sin\omega)}\left(\frac{t}{l}\right), \tag{1}$$

where ω is the angle of the inclined strut to the horizontal, see Fig. 10(a). For a regular honeycomb, ω equals $\pi/6$. Upon neglecting axial stretch of the struts, and upon taking P as the load on each vertical strut, we analyse one half of a beam inclined to the loading direction using Timoshenko beam theory, and apply symmetry boundary conditions, as illustrated in Fig. 10(b). The beam of length $l/2$ is built-in at its left-hand end, labelled $L1$, and is subjected to an end load $P/2$ at its point of inflection ($M = 0$), at location $L2$. The co-ordinate along the beam mid-surface is x. The bending moment along the beam $M(x)$ and shear force $Q(x)$ are given by:

$$M(x) = \frac{P}{2}\left(\frac{l}{2} - x\right)\cos\omega, \tag{2}$$

and

$$Q(x) = \frac{P}{2}\cos\omega, \tag{3}$$

respectively. Now, write ϕ as the angle of rotation of the normal to the mid-surface and w as the transverse displacement of the mid-surface. Then, Timoshenko beam theory [31] for a bundle of axial Young's modulus E_B and shear modulus G_B states that:

$$M(x) = E_B I\frac{\partial\phi}{\partial x}, \tag{4}$$

and

$$Q(x) = sAG_B\left(-\phi + \frac{\partial w}{\partial x}\right), \tag{5}$$

where I is the second moment of area, A the cross-sectional area, and the shear coefficient equals $s = 8/9$ [31]. We substitute Eq. (4) into (2) and integrate to obtain

$$\phi = \frac{x(l-x)\cdot P\cos\omega}{4E_B I}. \tag{6}$$

Substitution of Eqs. (6) and (3) into (5), followed by rearrangement and integration, yields

$$w = \frac{Px\cos\omega}{2sAG_B} + \frac{\left(\frac{x^2 l}{2} - \frac{x^3}{3}\right)\cdot P\cos\omega}{4E_B I}. \tag{7}$$

Since $\delta = w\left(x = \frac{l}{2}\right)$, we find that

$$\delta = \left(\frac{l}{4sAG_B} + \frac{l^3}{48E_B I}\right)P\cos\omega, \tag{8}$$

and the macroscopic strain ϵ^∞ in the direction of loading follows immediately as

$$\epsilon^\infty = \frac{2\delta\cos\omega}{(1+\sin\omega)\,l}. \tag{9}$$

Now, the macroscopic stress σ^∞ is given by $\sigma^\infty = P/(2lb\cos\omega)$, and upon making the substitution for the bundle area $A = tb$, and the second moment of area $I = bt^3/12$, the macroscopic modulus $E_{Mat} = \sigma^\infty/\epsilon^\infty$ reads

$$E_{Mat} = \frac{1+\sin\omega}{\cos^3\omega}\left[\frac{1}{sG_B}\left(\frac{l}{t}\right) + \frac{1}{E_B}\left(\frac{l}{t}\right)^3\right]^{-1}. \tag{10}$$

It remains to estimate the shear modulus G_B and axial modulus E_B for a bundle. Whilst the axial bundle modulus derives from covalent bonding within the CNT wall, the shear modulus is dictated by the much more compliant van-der-Waals bonding between adjacent CNTs. We follow the approach of [18] in estimating the axial bundle modulus as $E_B = (\rho_B/\rho_w)E_w$ where $\rho_w = 2200$ kg/m^3 (i.e. that of graphene at an interlayer spacing of 0.34 nm). For $E_w = 1$ TPa, it follows that $E_B = 680$ GPa. Values for G_B in literature have been deduced from in-situ 3-point bending tests [16,17], and from thermal vibration [32], varying from 0.7 to 6.5 GPa ± 50%.

Our measured mat modulus of 3.3 GPa from unloading tests and assumed value for E_B implies $G_B = 9.5$ GPa via Eq. (10), which is within the range of experimental measurements [16]. Inspection of Eq. (10) reveals the relative contribution of the shear and bending deformation to the macroscopic modulus. Since $sG_B \ll E_B(t/l)^2$, it is clear that the shear modulus of the CNT bundle dominates the deformation, as opposed to the stiffer covalent bonding along the CNT walls.

Now consider the tensile yield strength of the hexagonal lattice. The tensile stress on the outermost fibre of the inclined strut, due to the bending moment $M(x)$ and axial tension, is given by $\sigma_B = Mt/2I + (P/2tb)\sin\omega$, whereas the average shear stress on the cross section due to the shear force $Q(x)$ is given by $\tau_B = Q(x)/A$. As the bending moment is greatest at the location labelled $L1$ on the inclined strut illustrated in Fig. 10(b), σ_B and τ_B have the following maximum values:

$$\sigma_B = \left(\frac{27}{4(1+\sin\omega)^2\overline{\rho}^2} + \frac{3\sin\omega}{2(1+\sin\omega)\overline{\rho}}\right)\sigma^{\infty}, \tag{11}$$

and

$$\tau_B = \left(\frac{3\cos\omega}{2\,(1+\sin\omega)\,\overline{\rho}}\right)\sigma^{\infty}. \tag{12}$$

The ratio between bundle tensile stress and average shear stress is given by

$$\frac{\sigma_B}{\tau_B} = \frac{9}{2\cos\omega(1+\sin\omega)\overline{\rho}} + \frac{\sin\omega}{\cos\omega}. \tag{13}$$

Now, for a relative density $\overline{\rho} = 0.25$ and $\omega = \pi/6$, it follows that $\sigma_B/\tau_B = 14.4$. If the ratio of bundle tensile strength σ_{Bf} to bundle shear strength τ_{bf} is greater than σ_B/τ_B, macroscopic yield will be limited by the bundle shear strength, rather than by the fracture of CNT walls. We argue that this is the case, on the basis that the ratio σ_{Bf}/τ_{Bf} is more than four times greater than σ_B/τ_B, with the following justification.

Tensile tests conducted on individual CNT bundles grown by the chemical vapour deposition process suggest that the wall fracture strength of individual CNTs σ_{wf} lies between 5.5 GPa and 25 GPa [22]. Assume that the bundle strength scales with the CNT wall strength σ_{wf} according to $\sigma_{Bf} = (\rho_B/\rho_w)\,\sigma_{wf}$, and take $\sigma_{wf} = 5.5$ GPa. Then, the bundle fracture strength equals $\sigma_{Bf} = 3.7$ GPa.

Now consider the CNT bundle shear strength τ_{Bf}. Values for the bond shear strength between CVD-grown tubes, as measured in the literature, vary from 0.04 MPa to 70 MPa [19,20], with values sensitive to the concentration of graphitic defects [20,33]. For adjacent pristine CNT surfaces with long overlap lengths, the bond shear strength lies between 30 MPa and 60 MPa [34]. Here, we shall assume the value $\tau_{Bf} = 60$ MPa, as this implies a macroscopic yield stress of 17 MPa from Eq. (12), close to our experimental measurements, and lies within the range of values reported in literature. Consequently, $\sigma_{Bf}/\tau_{Bf} = 62$, and we conclude that the macroscopic yield strength is limited by the bundle shear strength.

Our conclusion that the shear strength of CNT bundles limits the macroscopic yield strength of direct-spun mats, as opposed to the bundle axial strength, is consistent with our observations of bundle deformation during in-situ testing, and explains why the random arrangement of CNT bundles within the mat results in a severe knockdown in mechanical properties when compared to those of individual CNTs in longitudinal tension.

5. Conclusions

The mechanical, electrical and thermal properties of direct-spun mats, fibres, and other CNT materials were compared over a wide range of densities. Characterisation of a commercially produced direct-spun mat revealed in-plane electrical conductivities of between 325 S/cm and 404 S/cm, elastic moduli of 3.0 GPa to 3.4 GPa, and an ultimate tensile strength between 30 MPa and 40 MPa. The through-thickness electrical conductivity and the mechanical properties of the bond between adjacent layers within the CNT mat were found to be much less than in-plane properties. Macroscopic deformation of CNT mat is accompanied by reorientation of the bundle network along the loading direction. A micromechanical model was developed to relate macroscopic direct-spun mat properties to those of CNT bundle network. It illustrates that the longitudinal shear deformation of CNT bundles dominates, and accounts for the knockdowns in CNT mat mechanical properties compared to those of an individual CNT in uniaxial tension.

Acknowledgements

The authors acknowledge the assistance of Simon Griggs of the Department of Materials Science for assistance with in-situ microscopy, Hadi Modarres and Michael De Volder of the Institute for Manufacturing for assistance with Thermogravimetric Analysis, and Tortech Nano Fibers Ltd. for supplying CNT mat. The authors acknowledge funding from the EPSRC project 'Advanced Nanotube Application and Manufacturing (ANAM) Initiative' under Grant No. EP/M015211/1.

Conflict of interest

The authors have no conflicts of interest to declare.

Appendix A. Composition of the Direct-Spun Mat

The chemical composition of the mat was determined by thermogravimetric analysis, conducted using a PerkinElmer TGA 4000. The temperature was held at 100 ° C to remove adsorbed moisture, then increased at a scan rate of 5 °C/min. The results revealed an Fe content of 6 wt.%, remainder CNT; the relationship between sample mass and temperature, and the rate of mass change with respect to temperature are plotted in Fig. A.1(a).

The Raman spectrum of the CNT mat was obtained with an EZRAMAN-N instrument, using a laser power of 50 mW, and 3 scans at 30 s integration time. A Raman spectrum of the CNT mat is illustrated in Fig. A.1(b). The high intensity G-band at 158 mm^{-1} corresponds to vibration of sp^2 bonds. Dividing the G-band intensity by that of the D-band at 134 mm^{-1} gives a G/D ratio of 4.5. The D-band results from the breathing mode of a six-fold aromatic ring, and cannot occur unless disorder is present, either in the crystalline structure of the CNT walls, or in the form of additional amorphous carbon materials [35,36]. The relatively high G/D ratio observed here indicates that neither of those defects are particularly prevalent. The absence of radial breathing modes at low frequency (<50 mm^{-1}) indicates that small diameter single- or double-walled CNTs are not present within the mat [35].

Bundle density was determined with helium pycnometry (performed by Quantachrome UK Ltd). This involves placing a CNT mat sample in a chamber of known volume, which is then purged of air and pressurised with helium gas. After the pressure of this chamber is measured, a valve is opened to link it with another chamber of known volume, initially at vacuum. After the pressure has stabilised, it is recorded; the perfect gas law is then used to calculate the sample volume from the measured gas pressures and known chamber volumes.

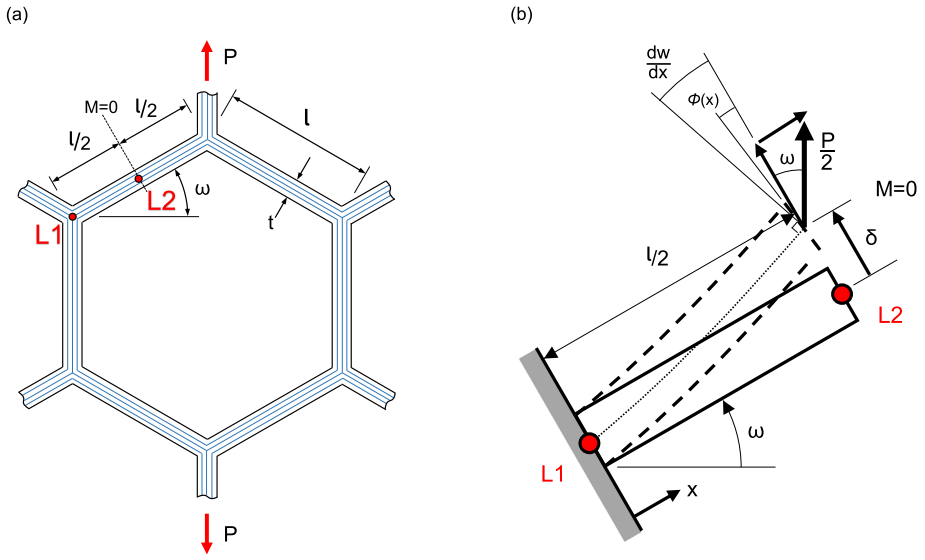

Fig. 10. (a) Geometry of a honeycomb unit cell of CNT bundle network microstructure (depth b into page), (b) loading and deformation of an inclined strut modelled with Timoshenko beam theory.

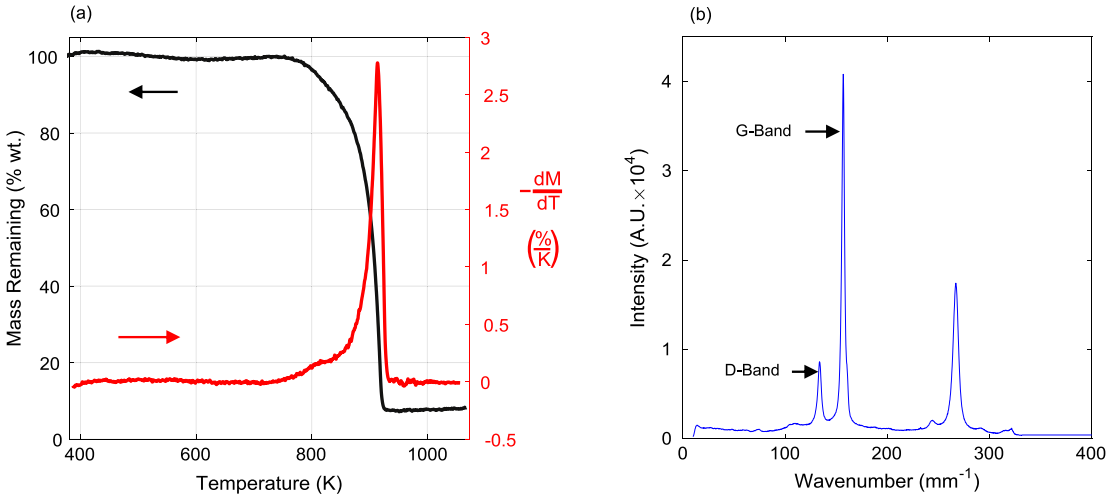

Fig. A.1. (a) Thermogravimetric analysis of CNT mat in air, (b) Raman spectra of CNT mat.

Appendix B. Supplementary data

Supplementary material related to this article can be found online at https://doi.org/10.1016/j.eml.2018.03.003.

References

[1] Michael F.L. De Volder, Sameh H. Tawfick, Ray H. Baughman, A. John Hart, Carbon nanotubes: present and future commercial applications, Science 339 (2013) 535–539.
[2] Bei Peng, Mark Locascio, Peter Zapol, Shuyou Li, Steven L. Mielke, George C. Schatz, Horacio D. Espinosa, Measurements of near-ultimate strength for multiwalled carbon nanotubes and irradiation-induced crosslinking improvements, Nature Nanotechnol. 3 (2008) 626–631.
[3] T.W. Ebbesen, H.J. Lezec, H. Hiura, J.W. Bennett, H.F. Ghaemi, T. Thio, Electrical conductivity of individual carbon nanotubes, Nature 382 (1996) 54–56.
[4] B.Q. Wei, R. Vajtai, P.M. Ajayan, Reliability and current carrying capacity of carbon nanotubes, Appl. Phys. Lett. 79 (2001) 1172–1174.
[5] Eric Pop, David Mann, Qian Wang, Kenneth Goodson, Hongjie Dai, Thermal conductance of an individual single-wall carbon nanotube above room temperature, Nano Lett. 6 (2006) 96–100.
[6] Ya-Li Li, Ian A. Kinloch, Alan H. Windle, Direct spinning of carbon nanotube fibers from chemical vapor deposition synthesis, Science 304 (2004) 276–278.
[7] Belén Alemán, Victor Reguero, Bartolomé Mas, Juan J. Vilatela, Strong carbon nanotube fibers by drawing inspiration from polymer fiber spinning, ACS Nano 9 (2015) 7392–7398.
[8] Lorna J. Gibson, Michael F. Ashby, Cellular Solids, second ed., Cambridge Solid State Sciences, 1999.
[9] Natnael Behabtu, Colin C. Young, Dmitri E. Tsentalovich, Olga Kleinerman, Xuan Wang, Anson W.K. Ma, Amram Bengio, Ron F. ter Waarbeek, Jorrit J. de Jong, Ron E. Hoogerwerf, Steven B. Fairchild, John B. Ferguson, Benji Maruyama, Junichiro Kono, Yeshayahu Talmon, Yachin Cohen, Marcin J. Otto, Matteo Pasquali, Strong, light, multifunctional fibers of carbon nanotubes with ultrahigh conductivity, Science 339 (2013) 182–186.
[10] T.S. Gspann, F.R. Smail, A.H. Windle, Spinning of carbon nanotube fibres using the floating catalyst high temperature route: purity issues and the critical role of sulphur, Faraday Discussions 173 (2014) 47–65.
[11] Christian Hoecker, Fiona Smail, Martin Pick, Adam Boies, The influence of carbon source and catalyst nanoparticles on CVD synthesis of CNT aerogel, Chem. Eng. J. 314 (2017) 388–395.
[12] Mukul Kumar, Yoshinori Ando, Chemical vapor deposition of carbon nanotubes: a review on growth mechanism and mass production, J. Nanosci. Nanotechnol. 10 (2010) 3739–3758.
[13] Shan Li, Xiaohua Zhang, Jingna Zhao, Fancheng Meng, Geng Xu, Zhenzhong Yong, Jingjing Jia, Zuoguang Zhang, Qingwen Li, Enhancement of carbon nanotube fibres using different solvents and polymers, Compos. Sci. Technol. 72 (2012) 1402–1407.

[14] Horacio D. Espinosa, Tobin Filleter, Mohammed Naraghi, Multiscale experimental mechanics of hierarchical carbon-based materials, Adv. Mater. 24 (2012) 2805–2823.
[15] Min-Feng Yu, Bradley S. Files, Sivaram Arepalli, Rodney S. Ruoff, Tensile loading of ropes of single wall carbon nanotubes and their mechanical properties, Phys. Rev. Lett. 84 (2000) 5552–5555.
[16] Jean-Paul Salvetat, G. Andrew D. Briggs, Jean-Marc Bonard, Revathi R. Bacsa, Andrezej J. Kulik, Elastic and shear moduli of single-walled carbon nanotube ropes, Phys. Rev. Lett. 82 (1999) 944–947.
[17] A. Kis, G. Csányi, J.-P. Salvetat, Thien-Nga Lee, E. Couteau, A.J. Kulik, W. Benoit, J. Brugger, L. Forró, Reinforcement of single-walled carbon nanotube bundles by intertube bridging, Nature Mater. 3 (2004) 153–157.
[18] J.Z. Liu, Q.-S. Zheng, L.-F. Wang, Q. Jiang, Mechanical properties of single-walled carbon nanotube bundles as bulk materials, J. Mech. Phys. Solids 53 (2005) 123–142.
[19] A. Kis, K. Jensen, S. Aloni, W. Mickelson, A. Zettl, Interlayer forces and ultralow sliding friction in multiwalled carbon nanotubes, Phys. Rev. Lett. 97 (2006) 025501.1-4.
[20] Osamu Suekane, Atsuko Nagataki, Hideki Mori, Yoshikazu Nakayama, Static friction force of carbon nanotube surfaces, Appl. Phys. Express 1 (2008) 064001.1-3.
[21] Mohammad Naraghi, Graham H. Bratzel, Tobin Filleter, Zhi An, Xiaoding Wei, SonBinh T. Nguyen, Markus J. Buehler, Horacio D. Espinosa, Atomistic investigation of load transfer between DWNT bundles "crosslinked" by PMMA oligomers, Adv. Funct. Mater. 23 (2012) 1883–1892.
[22] Mohammad Naraghi, Tobin Filleter, Alexander Moravsky, Mark Locascio, Raouf O. Loutfy, Horacio D. Espinosa, A multiscale study of high performance double-walled nanotube-polymer fibers, ACS Nano 4 (2010) 6463–6476.
[23] Yuanyuan Shang, Ying Wang, Shuhiu Li, Chunfei Hua, Mingchu Zou, Anyuan Cao, High-strength carbon nanotibers by twist-induced self-strengthening, Carbon 119 (2017) 47–55.
[24] Rebekah Downes, Shaokai Wang, David Haldane, Andrew Moench, Richard Liang, Strain-induced alignment mechanisms of carbon nanotube networks, Adv. Energy Mater. 17 (2015) 349–358.
[25] Fujun Xu, Baochun Wei, Wei Liu, Hongfei Zhu, Yongyi Zhang, Yiping Qiu, In-plane mechanical properties of carbon nanotube films fabricated by floating catalyst chemical vapor decomposition, J. Mater. Sci. 50 (2015) 8166–8174.
[26] Agnieszka Lekawa-Raus, Krzysztof K.K. Koziol, Alan H. Windle, Piezoresistive effect in carbon nanotube fibers, ACS Nano 8 (2014) 11214–11224.
[27] Standard Test Method for Tear-Propagation Resistance (Trouser Tear) of Plastic Film and Thin Sheeting by a Single-Tear Method, ASTM D1938-14. ASTM International, West Conshohocken, PA, 2014.
[28] H.W. Greensmith, A.G. Thomas, Rupture of rubber. 3. Determination of tear properties, J. Polym. Sci. 18 (1955) 189–200.
[29] Standard Test Method for Peel Resistance of Adhesives (T-Peel Test), ASTM D1876-08. ASTM International, West Conshohocken, PA, 2015.
[30] V.S. Deshpande, M.F. Ashby, N.A. Fleck, Foam topology: bending versus stretching dominated architectures, Acta Mater. 49 (2001) 1035–1040.
[31] S. Timoshenko, J.N. Goodier, Theory of Elasticity, McGraw-Hill, 1970.
[32] J.C. Lasjaunias, K. Biljakovic, P. Monceau, J.L. Sauvajol, Low-energy vibrational excitations in carbon nanotubes studied by heat capacity, Nanotechnology 14 (2003) 998–1003.
[33] Jeffrey T. Paci, Al'ona Furmanchuk, Horacio D. Espinosa, George C. Schatz, Shear and friction between carbon nanotubes in bundles and yarns, Nano Lett. 14 (2014) 3147–6138.
[34] Xiaoding Wei, Mohammad Naraghi, Horacio D. Espinosa, Optimal length scales emerging from shear load transfer in natural materials: application to carbon-based nanocomposite design, ACS Nano 6 (2012) 2333–2344.
[35] A. Jorio, M.A. Pimenta, A.G. Souza Filho, R. Saito, G. Dresselhaus, M.S. Dresselhaus, Characterizing carbon nanotube samples with resonance raman scattering, New J. Phys. 5 (2003) 139.1-17.
[36] A.C. Ferrari, J. Robertson, Interpretation of Raman spectra of disordered and amorphous carbon, Phys. Rev. B 61 (2000) 14095.